PAPER

Effect of Br content on phase stability and performance of $H_2N{=}CHNH_2Pb(I_{1-x}\,Br_{\,x}\,)_3$ perovskite thin films

To cite this article: Xiaojie Ni *et al* 2019 *Nanotechnology* **30** 165402

IOP Publishing Nanotechnology
Nanotechnology 30 (2019) 165402 (12pp) https://doi.org/10.1088/1361-6528/aafeb6

Effect of Br content on phase stability and performance of $H_2N{=}CHNH_2Pb(I_{1-x}Br_x)_3$ perovskite thin films

Xiaojie Ni[1,4], Lei Lei[2,3,4], Yu Yu[2,3], Junjie Xie[2], Ming Li[3], Songwang Yang[2,5], Mei Wang[1], Jiandang Liu[1], Hongjun Zhang[1] and Bangjiao Ye[1,5]

[1] State Key Laboratory of Particle Detection and Electronics, University of Science and Technology of China, Hefei 230026, People's Republic of China
[2] CAS Key Laboratory of Materials for Energy Conversion, Shanghai Institute of Ceramics, Chinese Academy of Sciences, Shanghai 200050, People's Republic of China
[3] Department of Mechanical, Materials and Manufacturing Engineering, University of Nottingham, University Park, Nottingham, NG7 2RD, United Kingdom

E-mail: swyang@mail.sic.ac.cn and bjye@ustc.edu.cn

Received 24 September 2018, revised 2 January 2019
Accepted for publication 15 January 2019
Published 13 February 2019

Abstract

Pristine and Br-doped $H_2N=CHNH_2Pb(I_{1-x}Br_x)_3$ ($FAPb(I_{1-x}Br_x)_3$, Br content $x = 0$, 0.05, 0.15, 0.2, 0.3, and 0.4) films were prepared. The effect of Br-doping on phase stability, defect density, and performance of $FAPb(I_{1-x}Br_x)_3$ was investigated by x-ray diffraction (XRD), scanning electron microscopy, ultraviolet–visible–near infrared absorbance spectroscopy, x-ray photoemission spectroscopy (XPS), Kelvin probe force microscopy (KPFM), positron annihilation spectroscopy, and current density–voltage (J–V) characteristics. The XRD measurements exhibit the enhancement of perovskite phase stability at $x = 0.05$. However, the phase stability decreases gradually with Br content (x) over 0.05. The increase of Br-doping content leads to the downshifting of both valence band (VB) position (indicated by XPS) and Fermi level (illustrated by KPFM). The energy level shifts are most probably due to the increase of Br 4p orbital content in VB and the change of self-doping levels. Doppler broadening spectra of positron annihilation radiation of the samples reveal that, the defect densities of Br-doped samples are much lower than that of pristine $FAPbI_3$. For $FAPb(I_{0.95}Br_{0.05})_3$ sample, a high photoelectric conversion efficiency of 17.12% (25.7% higher than that of undoped sample) is successfully achieved. The significant enhancement of photoelectric conversion efficiency realized by Br-doping is attributed to the improvement of morphology, high phase stability, and low defect densities.

Supplementary material for this article is available online

Keywords: formamidinium lead halide, Br doping, positron annihilation spectroscopy, perovskite solar cells

(Some figures may appear in colour only in the online journal)

1. Introduction

The global power consumption is soaring with the coming of age of artificial intelligence. Traditional power supply approaches based on fossil fuels are increasingly unsatisfactory. On one hand, fossil fuels are unsustainable. On the other hand, the burning

[4] These authors contributed equally to this work and should be regard as co-first authors.
[5] Authors to whom any correspondence should be addressed.

process inevitably leads to a high emission level of pollutants and carbon dioxide to atmospheric environment. As a result, the ecosystem bears increasing stresses. The gradual replacement of conventional energy is an unstoppable trend. Among various renewable energy sources, solar energy is highly competitive and likely to have a higher market share in the future.

The main technology to utilize solar power is converting it into electricity. A solar cell is the device which can directly convert solar light into electricity. Among a variety of solar devices, perovskite solar cell (PSC) is the first technology that combines simple fabrication processes [1–4] with high power conversion efficiencies (PCE) [5–7]. The active material alkali lead halides (ALHs) are nearly ideal materials for the photovoltaic applications, especially in terms of element abundance, processability, energy, and production cost per watt. Two types of ALHs are most widely used in the conversion from solar power to electricity: $CH_3NH_3PbI_3$ ($MAPbI_3$) [8–23] and $H_2N{=}CHNH_2PbI_3$ ($FAPbI_3$) [24–34]. The former has a stable perovskite phase at room temperature and is easy to prepare with solution processes. However, the bandgap (powder: 1.55 eV [35], film: 1.59 eV [36]) is slightly wide according to Schockley–Queisser limit [37]. Besides, the heat stability is inferior. Compared to $MAPbI_3$, $FAPbI_3$ has more favorable bandgap (powder: 1.48 eV [38], film: 1.52 eV [36]) and better heat stability [38, 39]. Although a high quality $FAPbI_3$ thin film is difficult to be prepared, it still attracts more attention than $MAPbI_3$.

Besides the inferior processability, $FAPbI_3$ also has an unstable perovskite phase [40–44] (α phase, cubic system, space group P_3m_3 [45]). At room temperature, metastable black phase of $FAPbI_3$ transforms to stable yellow phase (δ phase, hexagonal system, space group $P6_3mc$). Co-doping of MA^+ and Br^- is found to be able to stabilize the α phase of $FAPbI_3$ effectively. High efficiency has been achieved by researchers based on $(FAPbI_3)_{1-x}(MAPbBr_3)_x$ [46]. Excellent light stability was realized by further doping with alkali metals [26, 47].

The compositional space of mixed perovskites has been investigated by Jesper Jacobsson [36]. The detailed influence of Br on the performance of $FAPbI_3$, however, remains pending. In this work, the influence of Br on perovskite morphology, phase stability, band position, defect density, and photovoltaic performance were studied. A low content of Br in mixed halide perovskite $FAPb(I_{1-x}Br_x)_3$ increases the stability of α phase. However, the perovskite phase stability notably decreases when Br contents are larger than 0.05. The origin of the phase stability change was analyzed based on the lattice energy and electronegativity of halide elements. The morphology evolution as a function of Br content was clarified. With the doping of Br, dense grains which are a larger size were observed. The absorbance spectra of $FAPb(I_{1-x}Br_x)_3$ films were recorded and analyzed. $FAPb(I_{1-x}Br_x)_3$ films with high Br content have low absorption for the wavelength ranges between 550 and 800 nm. The low absorbance of $FAPb(I_{1-x}Br_x)_3$ films reveals the low perovskite phase content for a high Br content. The defect density of $FAPb(I_{1-x}Br_x)_3$ films was studied by positron annihilation spectroscopy. High defect density was observed at the surface of perovskite films. The defect densities of Br-doped samples are much lower than those of $FAPbI_3$ due to the enhanced film quality. With the increase of Br content, the defect densities of $FAPb(I_{1-x}Br_x)_3$ films decrease. When the contents of bromine are 0.05, 0.15, 0.2, the defect densities are almost the same. For the Br contents larger than 0.2, the defect density decreases drastically. This indicates that fewer positrons were captured and annihilated in $FAPb(I_{1-x}Br_x)_3$ films with the decrease of α/δ phase content ratio. The photovoltaic performances of $FAPb(I_{1-x}Br_x)_3$ films were studied. With high absorbance and low defect density, the highest efficiency of 17.12% is achieved for $FAPb(I_{0.95}Br_{0.05})_3$ film. The PCE increases by 25.7% compared to that of $FAPbI_3$ film.

2. Experiments and methods

2.1. Experiments

Fluorine-doped tin oxide (FTO) coated glass slides and glass substrates were successively cleaned by ultrasonic bath with detergent, deionized water, acetone, and ethanol. The substrates were ultraviolet-ozone treated to remove organic residuals before use. Compact TiO_2 (c-TiO_2) was deposited on FTO with a sol–gel method by spin coating (at a speed of 3000 rpm for 20 s). The precursor was prepared by adding an ethanol solution of hydrochloride acid in a 0.3 mol l^{-1} titanium isopropoxide and acetylacetone ethanol solution. The as-cast films were calcined at 510 °C for 30 min The films were treated with a 30 mM (m mol l^{-1}) $TiCl_4$ aqueous solution at 70 °C for 40 min After cooling down to room temperature, c-TiO_2 films were rinsed by deionized water and ethanol. The substrates were calcined again at 510 °C for 30 min after dried by air flow. A mesoporous TiO_2 (m-TiO_2) layer was fabricated with a home-made paste containing 18 wt% TiO_2 nanoparticles (25–30 nm in size), ethyl cellulose (as a pore-forming agent) and terpineol (as a dispersant). To fabricate a mesoporous scaffold with a thickness of about 150 nm, the paste was diluted by adding ethanol. The paste/ethanol weight ratio was 1:5. To ensure homogeneous dispersion of TiO_2 nanoparticles in ethanol, ultrasonic treatment was conducted for 6 h. The as-obtained suspension was cast on compact TiO_2 film at a speed of 3000 rpm for 20 s. The films were calcined at 510 °C for 30 min to remove organic components. The mesoporous scaffold was ultraviolet-ozone treated for 15 min before the deposition of perovskite layer.

Perovskite precursor solutions were prepared by mixing formamidinium iodide (FAI, TCI, 99%), lead iodide (PbI_2, Aladdin, 99%), and lead bromide ($PbBr_2$, Aladdin, 99%) in dimethyl sulfoxide (DMSO) and N, N-dimethyl formamide (DMF) (volume ratio 1:4). The weight of FAI was 0.258 g and the mixed solvent volume was 1 ml. The weights of PbI_2 and $PbBr_2$ were listed in table 1. The solutions were spin coated at 2000 rpm for 10 s and then at 5000 rpm for 30 s in a dry room (at a fixed temperature of 20 °C, relative humidity $< 1\%$). Chlorobenzene (0.2 ml) was dripped on the rotating substrate at 20 s before the end of the rotation. The

Table 1. The weights of PbI_2 and $PbBr_2$ for perovskite precursor solutions with different Br content.

Br content (x)	0	0.05	0.15	0.2	0.3	0.4
PbI_2 (g)	0.6915	0.6396	0.5359	0.4841	0.3803	0.2766
$PbBr_2$ (g)	0.0000	0.0413	0.1239	0.1652	0.2477	0.3303

as-cast films were annealed on a hot plate at 160 °C for 10 min. The perovskite films were cooled at room temperature for 30 min and a spiro-OMeTAD (Merck) solution was spin coated at 4000 rpm for 30 s. The solution was prepared by dissolving 72.3 mg spiro-OMeTAD in 1 ml chlorobenzene with 21.8 μl bis(trifluoromethylsulfonyl)imide lithium salt (Li-TFSI, J&K Chemicals) stock solution (520 mg ml^{-1} in acetonitrile) and 17.6 μl 4-tert-butylpyridine (TBP, Sigma Aldrich). The hole transport material (HTM) coated perovskite films were shaded and stocked in dry air for 12 h to partly oxidizing spiro-OMeTAD. A 120 nm thick Ag was deposited on HTM by thermal evaporation as back contact. A tungsten boat was used as a heating source. The vacuum was maintained below 10^{-5} tor during the deposition. The deposition rate was 1–3 Å s^{-1}. Metal masks were used to fix the active area as 0.07 cm^2.

2.2. Methods

X-ray diffraction (XRD) characterization was conducted with a Rigaku Ultima IV diffractometer. Grazing mode with scan step and scan speed of 0.02 and 4° min^{-1} was used. The films were sealed with Scotch magic tapes to avoid phase transition during the test. The lattice energy of $FAPbI_3$ and $FAPbBr_3$ were calculated with the free software Vesta.

The morphology of perovskite films was checked by scanning electron microscopy (SEM, JEOL 7100). The grain size statistics were obtained by measuring the maximum horizontal length of perovskite grains. The software used in this work was nanomeasure. One SEM image was analyzed with a sample size of 250–300. The surface roughness of perovskite films were measured by AFM (CEKO, SPI-3800N). To check the phase purity, perovskite films were directly cast on the glass and annealed at 160 °C for 10 min.

The optical absorbance of perovskite films was recorded by an ultraviolet–visible–near-infrared (UV–vis–NIR) spectrometer (Shimadzu UV-2550 PC). The bandgaps of light absorber were calculated from the $(\alpha h\nu)^2$-$h\nu$ plot by extrapolating the linear edge of $(\alpha h\nu)^2$ to zero, where α and $h\nu$ are the absorption coefficient of perovskite and the photon energy of incident light, respectively.

The valence spectra of $FAPb(I_{1-x}Br_x)_3$ films were characterized by x-ray photoemission spectroscopy (XPS, Thermo Scientific, ESCALAB 250). Al Kα target was used to yield an x-ray with 1486.6 eV photon energy. The energy step size was 0.05 eV and the photon–electron pass energy of analyzer was 30.0 eV. Fixed retarding ratio mode was used since valance peaks have low intensities. The spectra positions were calibrated with the C 1s peak positions to ensure the zero binding energy points were the Fermi levels of the samples. The Fermi levels of perovskite films were checked by Kelvin probe force microscopy (KPFM, Bruker, Dimension Icon). The work function of the conductive tip was calibrated with a fresh surface of highly ordered pyrolytic graphite. The average surface potential of a 10 by 10 μm area was used to calculate the work function of the samples.

The Doppler broadening of positron annihilation spectroscopy were collected by a slow positron beam spectrometer which was developed by State Key Laboratory of Particle Detection and Electronics, University of Science and Technology of China. The Doppler broadening spectroscopy has unique advantages to study the defect densities of thin films. After thermalization (kinetic energy dropping to thermal energy level in 2–3 picoseconds), positrons diffuse arbitrarily in the sample. During the diffusion process, positrons are easily trapped by defects and eventually annihilate with the electrons around the defects. It reflects the variation of defect concentration with depth of positrons implantation in sample. The Doppler broadening spectra were analyzed by the VEPFIT program [48, 49]. The energy of incident positron beam is continuously tunable between 0 and 20 keV. S parameter which is defined as the ratio between central area (511 $\pm$ 0.802 keV) and total peak area, reflects the annihilation of positrons with low-momentum valence electrons. The increase of S parameter indicates the increase of defect densities (the fraction of valence electrons around defects is higher than those in the defect-free regions) in samples.

The current density–voltage (J–V) characteristics of PSCs were measured by a source meter (Keithley 2400). The incident light applied was a simulating standard AM 1.5 G spectrum generated by a xenon lamp (Newport 94083 A). The intensity of incident light was calibrated by an AAA class Si solar cell (Oriel-91150). A decreasing bias from 1.2 to 0 V was applied to PSCs with 451 steps. The hold time on each step before the current test was 50 ms and the interval time between bias steps was 10 ms, corresponding to a scanning rate of 40 mV s^{-1}.

3. Results and discussion

3.1. Influence of Br on phase composition and stability

The phase composition and α phase (cubic Pm3m space group) stability of $FAPb(I_{1-x}Br_x)_3$ were investigated by XRD. The results are presented in figure 1. The main peak of α phase that is near 14° increases first, and then decreases with Br-doping. When Br content is low ($x \leqslant 0.05$), α phase is stabilized by Br-doping. When Br content (x) is over 0.15, the intensity of α phase main peak decreases with the increase of Br content. This reveals that the over-doping of Br in $FAPbI_3$ would decrease the stability of the perovskite phase. According to

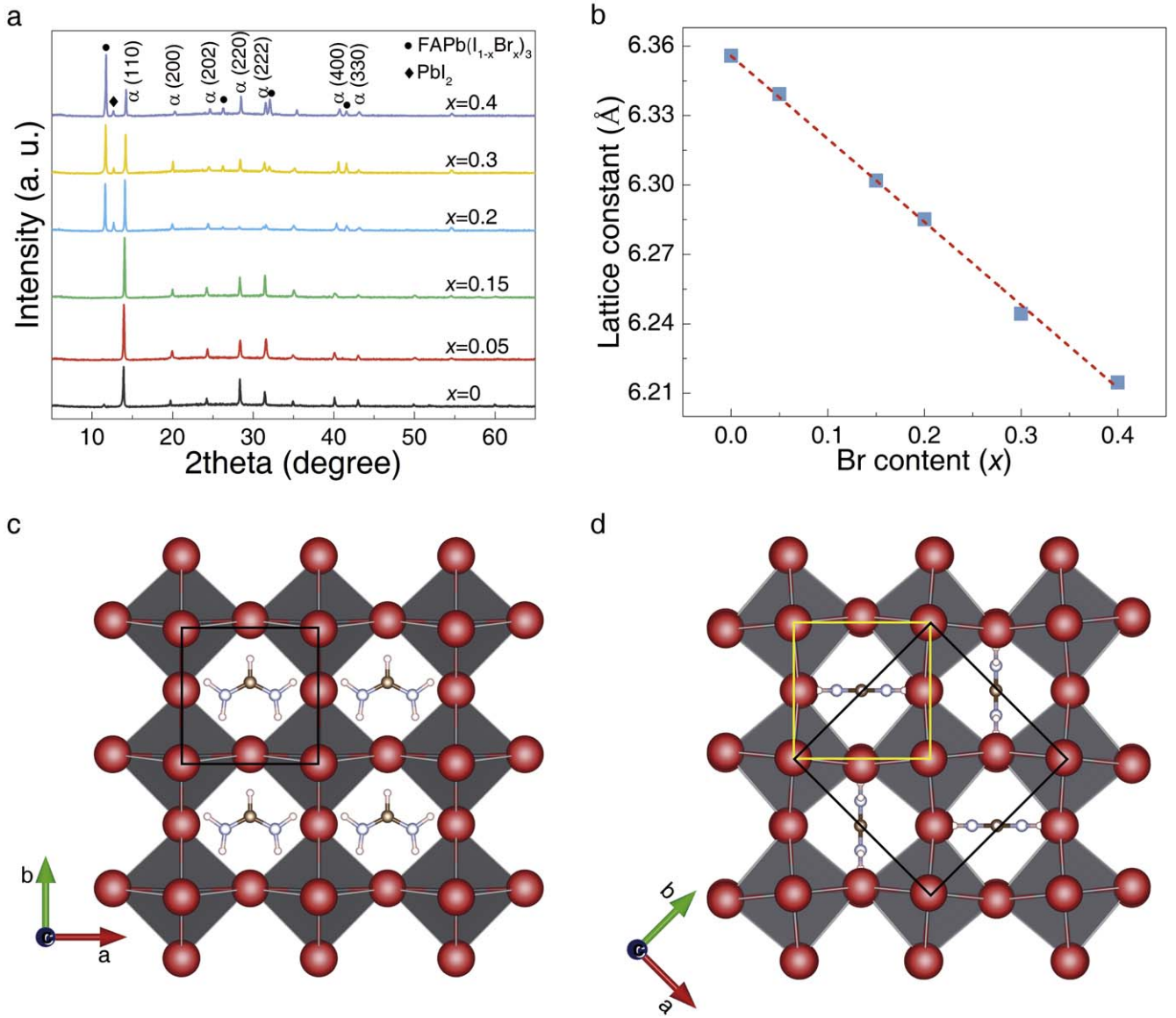

Figure 1. (a) The XRD patterns of $FAPb(I_{1-x}Br_x)_3$ films on glass annealed at 160 °C for 10 min. (b) The lattice constants of $FAPb(I_{1-x}Br_x)_3$ films calculated by (110) diffraction peak position in (a). Illustration of $FAPbI_3$ lattices: (c) the ideal cubic structure, and (d) the slightly tilted structure in reality. The primitive cells are highlighted with black squares. For the real structure, the pseudo-cubic cell is highlighted with a yellow square.

previous studies, $FAPbBr_3$ has a cubic structure of Pm3m as well with a smaller lattice constant ($\boldsymbol{a}$ = 5.9944 Å of $FAPbBr_3$ versus $\boldsymbol{a}$ = 6.3573 Å of $FAPbI_3$[50]).

Due to the tilting of the PbX_6 octahedral frame, the symmetry degrades from cubic (figure 1(c)) to tetragonal (figure 1(d)). To compare the lattice parameters, the pseudo-cubic cell was used (figure 1(d)). Because the coordinate system of the tetragonal primitive cell has a 45° angle with the cubic primitive cell, the (100) plane of cubic cell replaces the (110) plane of tetragonal structure (figure 1(d)). The lattice constants of the tetragonal real cell and pseudocubic cubic cell hence have the following relation [51–53]:

$$\boldsymbol{a_c} = \sqrt{2}\boldsymbol{a_t}/2;\ \ \boldsymbol{c_c} = \boldsymbol{c_t}/2, \tag{1}$$

where $\boldsymbol{a_c}$, $\boldsymbol{c_c}$, $\boldsymbol{a_t}$, and $\boldsymbol{c_t}$ are the lattice constants of pseudo-cubic and tetragonal structure respectively. For the pseudocubic structure, $\boldsymbol{a_c} = \boldsymbol{c_c}$. The lattice parameters of $FAPb(I_{1-x}Br_x)_3$ were calculated according to the positions of (110) peak near 14°. As presented in figure 1(b), the lattice constant of $FAPb(I_{1-x}Br_x)_3$ is linear relevant to the Br content. It indicates that the Br content in the perovskite phase is not influenced by the phase segregation. The bromine is incorporated in the lattice during calcination and homogeneously distributed. While during the cooling process, the high temperature stable α phase starts to transform to low temperature stable δ phase. During the phase transition, Br is hard to move because of the low temperature. Hence, Br is nearly homogeneously distributed in the films in spite of the phase segregation. It should be noted that the phase segregation in this system is caused by the low stability of α phase instead of solubility limit of Br in the perovskite lattice. The linear relation between lattice constant and Br content indicates the formation of solid solution in the

mixed halogen films. However, the lower phase stability of high Br-doping content films makes the phase transition speed faster and hence forms more δ phase.

To understand the influence of Br on the perovskite phase stability, we have calculated the Goldschmidt tolerance factor of $FAPb(I_{1-x}Br_x)_3$. Goldschmidt tolerance factor $\boldsymbol{t}$ was calculated according to the following equation [54]:

$$\boldsymbol{t} = (\boldsymbol{r_A} + \boldsymbol{r_X})/\sqrt{2}\,(\boldsymbol{r_B} + \boldsymbol{r_X}), \quad (2)$$

where $\boldsymbol{r_A}$, $\boldsymbol{r_B}$ and $\boldsymbol{r_X}$ are the radii of A site cation FA^+ (2.53 Å), B site cation Pb^{2+} (1.19 Å) and X site anions I^- (2.20 Å) or Br^- (1.96 Å) respectively. The $\boldsymbol{t}$ values for $FAPbI_3$ and $FAPbBr_3$ are 0.987 and 1.008. With a tolerance factor close to 1, $FAPbBr_3$ forms an ideal cubic perovskite structure. To understand the phase stability of $FAPb(I_{1-x}Br_x)_3$, average tolerance factor was calculated with the following equation:

$$\bar{\boldsymbol{t}} = (1 - \boldsymbol{x})\boldsymbol{t}_{\mathrm{I}} + \boldsymbol{x}\boldsymbol{t}_{\mathrm{Br}}, \quad (3)$$

where $\boldsymbol{t}_{\mathrm{I}}$ and $\boldsymbol{t}_{\mathrm{Br}}$ are the tolerance factors of $FAPbI_3$ and $FAPbBr_3$, $\boldsymbol{x}$ is the Br content. The average tolerance factor located in the range of 0.987–0.995 with a doping range of 0–0.4. With a slightly small $\boldsymbol{t}$ value, $FAPbI_3$ should be able to form a stable perovskite structure. However, the perovskite phase stability is reduced with the increase of Br content.

The electrostatic energy (lattice energy) per asymmetric unit of $FAPbI_3$ and $FAPbBr_3$ were calculated as −23.52 and −24.97 eV/cell. The lower stability of perovskite phase of $FAPbI_3$ is attributed to the high Madelung electrostatic potential. With a slightly lower lattice energy, $FAPbBr_3$ is easier to form and has higher stability. The electronegativity differences of Pb–I and Pb–Br are 0.79 and 1.09, Pb–Br bonding is hence more ionic. The actual lattice energy of $FAPbI_3$ would be higher and perovskite phase of $FAPbI_3$ would be less stable. With a large effective radius, iodine-based perovskites have lower electrostatic stabilization. In other words, due to the lower electronegativity of iodine, Pb–I bonds are more covalent in contrast with Pb–Br bonds. With stronger Pb–X ionic bonding, the 3D $PbBr_6$ framework is more stable.

With the introduction of Br in the $FAPbI_3$ lattice, the lattice constant decreases accordingly and the PbX_6 is tilted and distorted due to the Pb–Br bond is shorter than Pb–I bond (figure 2(a)). When Br content is low, the slightly decreased lattice constant would stabilize the corner shared PbX_6 frame because of the increased electrostatic forces between ions. When Br content is high, the tilting of PbX_6 will be prominent. When Br content is in the range of 0.3–0.4, about one-third of iodine was replaced by Br. That means two Pb–I bonds in PbI_6 were replaced with Pb–Br bonds. The tilting of PbX_6 and Pb–Br bonds' introduction caused the deformation of octahedral interstices. Some interstices expanded while the others shrank. The contractive cavities are too small to hold FA^+ ions. The FA–I bond lengths in α and δ phases are $\sqrt{2}\boldsymbol{a}/2$ (4.50 Å) and $\sqrt{3}\boldsymbol{a}$ (5.00 Å) (figures 2(b) and (c)). With a large FA–X bond length, the δ phase has enough spaces for FA^+ ions despite Pb–I bonds are partly replaced with shorter Pb–Br bonds. Meanwhile, the serious tilting of PbX_6 will decrease the distance between iodine ions. The decreased distance increases the repelling forces between iodine ions. The repelling electrostatic force between halide ions and the expansion trend of the PbX_6 framework to contain FA^+ ions compel the rearrangement of PbX_6 octahedrons (transits from corner sharing 3D framework to isolated face sharing chains). Hence, the stability of α phase decreases dramatically with high Br-doping content. The incorporation of Br in the perovskite lattice has a significance on the heat stability as well. XRD was used to check the thermal stability of $FAPb(I_{1-x}Br_x)_3$ films (figure S1 is available online at stacks.iop.org/NANO/30/165402/mmedia). Perovskite films with different Br content were calcinated at 150 °C for 8 h and XRD patterns were recorded. The main peak intensity ratio of PbI_2 to $FAPb(I_{1-x}Br_x)_3$ has a minimum ratio at a Br content of 0.05 indicating the best heat stability.

3.2. Influence of Br on morphology

The top view morphologies of perovskite films with different Br content are shown in figure 3. Without Br-doping, perovskite film has a rough surface, while perovskite films are flat after Br-doping. The surface roughness difference was further confirmed by the AFM characterization (figures S3 and S4). The root mean square (rms) roughness decreased from 85.57 nm for pristine film to 44.97 nm with a 0.05 Br-doping content. A minimum roughness of 30.4 nm was obtained with a Br-doping content of 0.15. Except for the difference of surface roughness, the grain size varies with the Br content. The grain size statistics were given in figure 4. The average grain size of $FAPbI_3$ is 223.19 nm. With Br-doping, the ratio of large grains increases. The average grain sizes of $FAPb(I_{1-x}Br_x)_3$ are 278.54, 287.29, 285.98, 246.14, and 231.54 nm respectively for $x = 0.05$, 0.15, 0.2, 0.3, and 0.4. As the statistics demonstrates, $FAPb(I_{0.85}Br_{0.15})_3$ has a largest average grain size. The elemental distribution of these films was checked by EDS (figure S1). The elements are nearly homogeneous detected despite phase segregation is observed for samples with high Br content. This indicates that the difference of Br content in α and δ phases of $FAPb(I_{1-x}Br_x)_3$ is negligible which is consistent with the lattice parameter data of the perovskite phase.

3.3. Influence of Br on optical property and energy levels

The vis–NIR absorbance spectra of $FAPb(I_{1-x}Br_x)_3$ films are shown in figure 5(a). With the increase of Br content, the absorption edge of $FAPb(I_{1-x}Br_x)_3$ has a blue shift. Bulk $FAPbI_3$ and $FAPbBr_3$ perovskites have bandgaps of 1.48 and 2.23 eV [50]. The wider bandgap of $FAPbBr_3$ compared to $FAPbI_3$ origins from the larger gap between Pb–X bonding and anti-bonding orbitals. With the introduction of Br, the proportion of Pb–Br bonding increases, yielding a gradually widen bandgap. The bandgaps of perovskite phase obtained by Tauc's plots are 1.55, 1.58, 1.62, 1.65, 1.74, and 1.74 eV for $x = 0$, 0.05, 0.15, 0.2, 0.3 and 0.4 respectively (figure 5(b)). The bandgap stops increasing after $x = 0.3$.

The energy level of $FAPb(I_{1-x}Br_x)_3$ with different Br content was clarified. According to the Fermi level measured

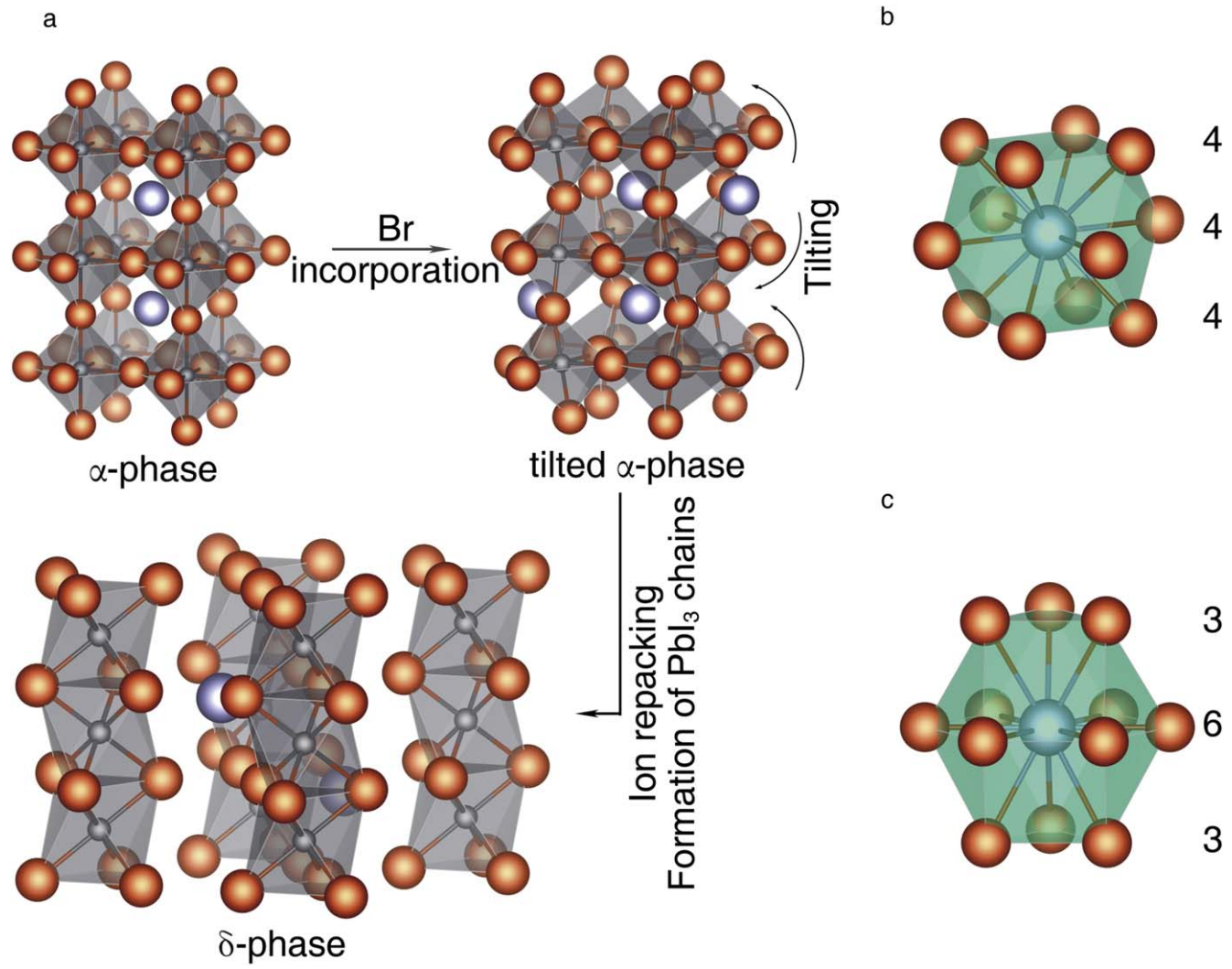

Figure 2. (a) Illustration of PbX_6 octahedron tilting after Br incorporation and α phase to δ phase transition. FA–X coordination in different $FAPb(I_{1-x}Br_x)_3$ phases: (b) FA–X tetradecahedron with six square faces and eight triangle faces in α phase, the cage is formed by halogen atoms with (4, 4, 4) packing, and (c) FA–X hexadecahedron with six square faces and ten triangle faces in δ phase, the cage is formed by halogen atoms with (3, 6, 3) packing.

by KPFM, the incorporation of Br deepens the Femi level of $FAPb(I_{1-x}Br_x)_3$. As shown in table 2, the Femi level decreases from −4.50 eV for $FAPbI_3$ to −4.65 eV for $FAPb(I_{0.6}Br_{0.4})_3$. The observed Fermi position versus VB position was illustrated in figure 5(d). The relative position reflects the doping level of perovskite materials. For intrinsic semiconductor without doping, the Fermi level locates near the middle of the bandgap. For highly doped semiconductors, the Fermi level generally locates very close to VB (*p*-type) or CB (*n*-type).

The downshift of Fermi level is mainly caused by the decrease of the self-doping level. The halide elements would evaporate during the heat treatment. Halogen vacancies would form accordingly and cause the self-doping of perovskite materials. The halogen vacancies are positively charged which are balanced by excess electrons in the lattice which shifts the quasi-Fermi levels upwards. The Br forms stronger bonding with Pb, and the probability of Pb–Br bond dissociation is lower. Except for the downshift of Fermi level, the VB position downshifts as well. The VB of $FAPb(I_{1-x}Br_x)_3$ deepens with the increase of Br content. According to previous studies on the band structure of perovskite, the VB of perovskite is mainly dominated by the *p* orbitals of halogen (I 5*p* or Br 4*p*) [55]. Hence, it is reasonable that the valance position downshifts with the increase of Br 4*p* content which has a lower energy. The CB of $FAPbI_3$ changed slightly after Br incorporation. CB of perovskite is mainly composed of Pb 6*p* orbitals. The shift may be a result of crystal structure and morphology difference.

3.4. Influence of Br on defect densities

The defect densities of perovskite films with different bromine content were characterized by PAS. The variation of *S* parameter (low-momentum valence electrons annihilation fraction) of $FAPb(I_{1-x}Br_x)_3$ as a function of positron energy is

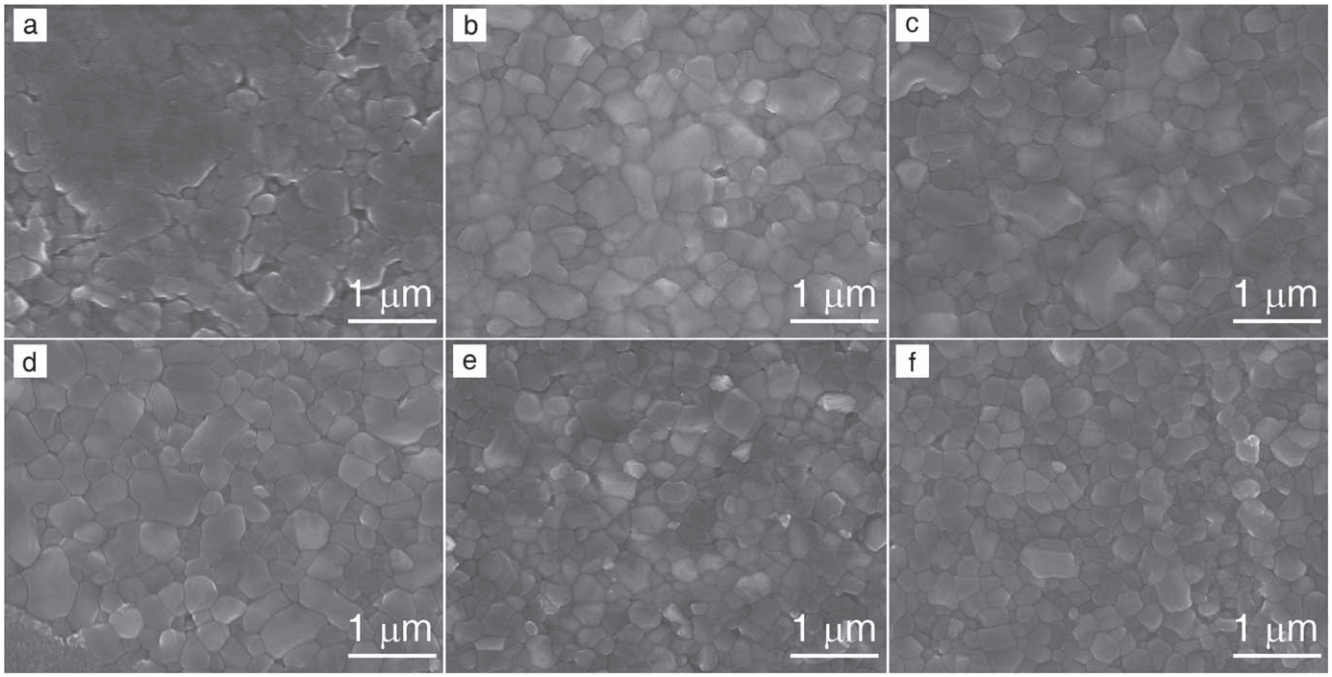

Figure 3. Top-view morphology of $FAPb(I_{1-x}Br_x)_3$: (a) $x = 0$, (b) $x = 0.05$, (c) $x = 0.15$, (d) $x = 0.2$, (e) $x = 0.3$, and (f) $x = 0.4$.

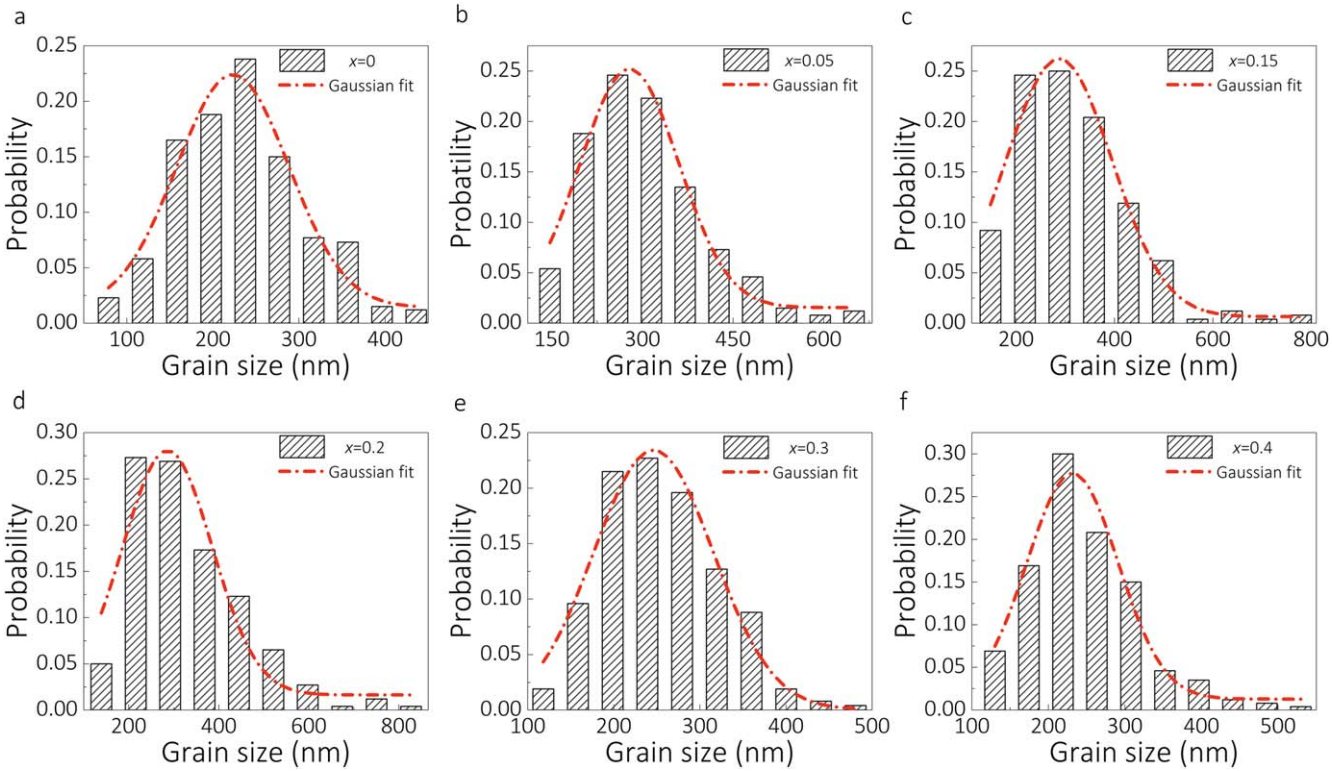

Figure 4. Grain size distribution of $FAPb(I_{1-x}Br_x)_3$ films: (a) $x = 0$, (b) $x = 0.05$, (c) $x = 0.15$, (d) $x = 0.2$, (e) $x = 0.3$, and (f) $x = 0.4$.

shown in figure 6(a). The depth distribution of positrons in the sample depends on the positron energy which follows the so-called Makhov distribution [56]:

$$P(z, E) = \frac{mz^{m-1}}{z_0^m} \exp\left[-\left(\frac{z}{z_0}\right)^m\right], \tag{4}$$

where m is a constant, $\mathbf{z}$ is the depth, $\boldsymbol{E}$ is the positron injection energy, $\mathbf{z}_0$ is a constant depends on the average injection depth of positron ($\bar{z}$):

$$z_0 = \frac{\bar{z}}{\Gamma\left[\left(\frac{1}{m}\right) + 1\right]} \tag{5}$$

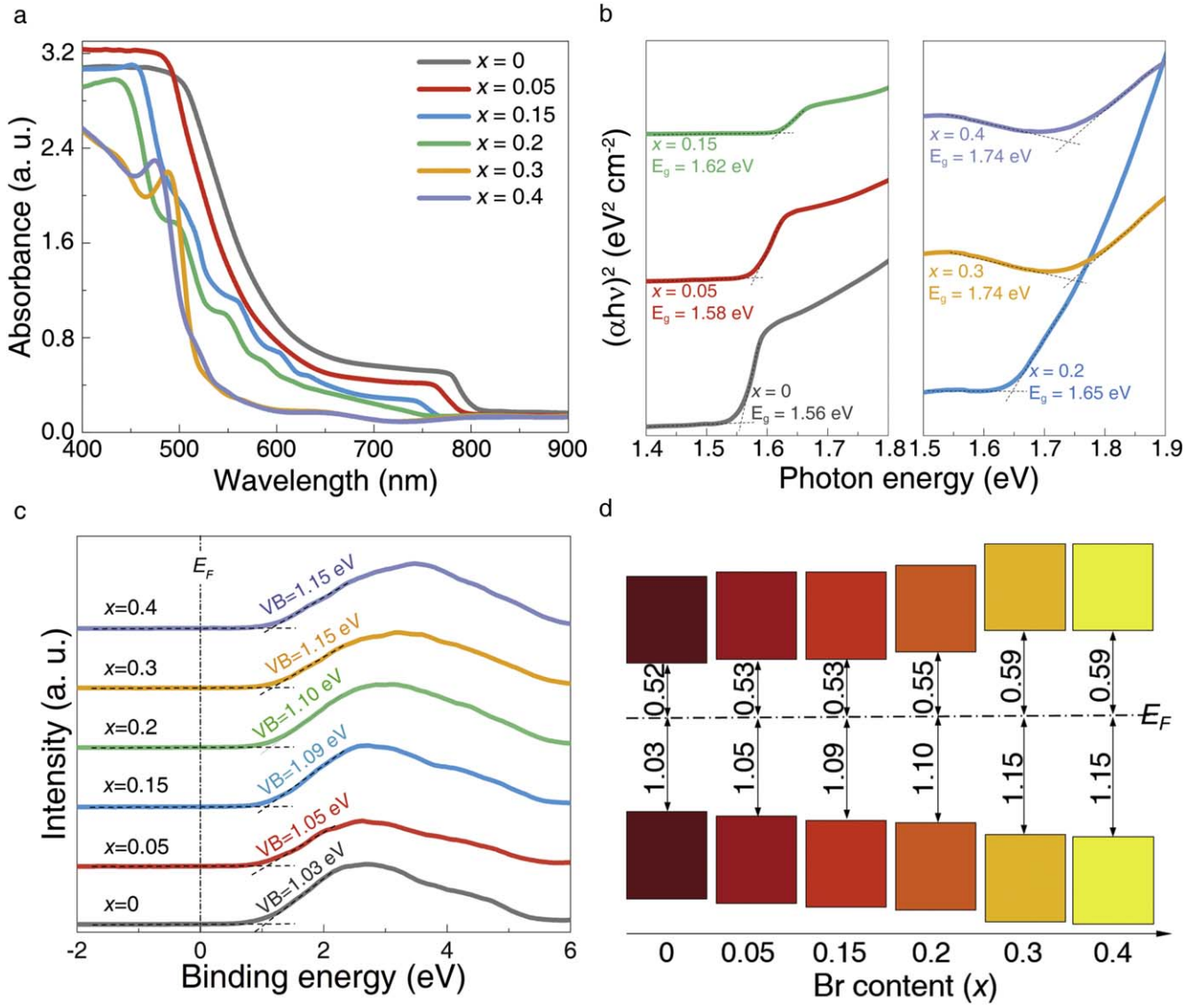

Figure 5. (a) The Vis–NIR transmittance spectra of FTO/c-TiO_2/meso-TiO_2/$FAPb(I_{1-x}Br_x)_3$ films. (b) Tauc's plot ($(\alpha h\nu)^2$-$h\nu$ relation) of FTO/c-TiO_2/meso-TiO_2/$FAPb(I_{1-x}Br_x)_3$ films, the E_g of different samples are obtained by extrapolating the linear edge of $(\alpha h\nu)^2$ to zero. (c) XPS valence spectra of FTO/c-TiO_2/meso-TiO_2/$FAPb(I_{1-x}Br_x)_3$ films, the energy scale is referenced to the Fermi level, E_F (0 eV). (d) The relative position of conduction band (CB) and valence band (VB) to Fermi level (E_F) of $FAPb(I_{1-x}Br_x)_3$ films.

$$\bar{z} = \frac{A}{\rho}E^n, \tag{6}$$

$$\Delta S/S = \frac{S_{\text{Br doped film}} - S_{\text{pristine film}}}{S_{\text{pristine film}}}. \tag{7}$$

where Γ is the gamma function, ρ is the density of the material, n and A are constants.

According to previous works, n and A can take the values of 1.667 and 2.58 $\mu g\,cm^{-2}\,keV^{-1.667}$, respectively [56, 57]. The densities of α-phase (4.101 $g\,cm^{-3}$) and δ-phase (4.096 $g\,cm^{-3}$) $FAPbI_3$ are close to each other [58]. To simplify the problem, the mean injection depth of positrons ($\bar{z}$) was calculated with the density of α-phase $FAPbI_3$. The calculated average injection depth was in the range from 0.6 nm ($E = 0.25$ keV) to 928.0 nm ($E = 20$ keV).

The relative S parameter ($\Delta S/S$) is defined by the following equation [59]:

The $\Delta S/S$ parameters (obtained by the VEPFIT program) versus injection positron energy are shown in figure 6(b). The low energy positrons ($E < 2$ keV) generally annihilate at the surface of materials. Surface annihilation leads to high S parameter values at low injection positron energy for all samples. Compared to Br-doped samples, the pristine $FAPbI_3$ sample has a higher surface annihilation fraction which is probably due to its smaller grain size and rougher surface. For the high injection energy that higher than 14 keV, a large fraction of positrons annihilate in TiO_2 or FTO substrates. This could be observed from figure 6(a) where the S parameters stop decreasing and start to increase slowly at the

Table 2. Summary of energy level positions and bandgap values of $FAPb(I_{1-x}Br_x)_3$ films.

Br content (x)	0	0.05	0.15	0.2	0.3	0.4
Fermi level (eV)	−4.50	−4.57	−4.60	−4.65	−4.65	−4.65
VB (eV)	−5.53	−5.62	−5.69	−5.75	−5.80	−5.80
Eg (eV)	1.55	1.58	1.62	1.65	1.74	1.74
CB (eV)	−3.98	−4.04	−4.07	−4.10	−4.06	−4.06

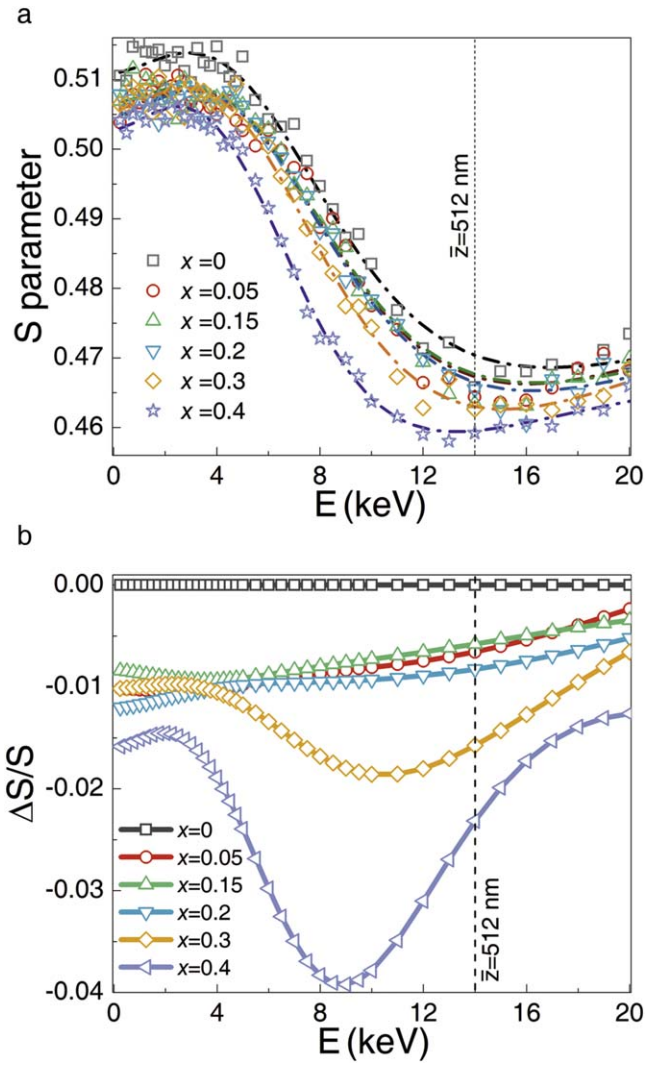

Figure 6. (a) The S parameter evolution with injection positron energy (E) of $FAPb(I_{1-x}Br_x)_3$ films, the dashed lines are fitted values obtained from the VEPFIT program. (b) $\Delta S/S$ (obtained by VEPFIT program) as a function of E in $FAPb(I_{1-x}Br_x)_3$ films.

positron energy near 14 keV (corresponding to the mean injection depth of 512 nm). The S parameters in the injection positron energy of 2–14 keV reveal the defect information of film body. According to the previous work, the incorporation of Br could increase the formation energy of vacancies [60]. Positrons are generally trapped in cation vacancies, since they are mostly negative charged. Because the halogen substitution is equivalent doping, the cation and anion vacancies form simultaneously. Figure 6(a) shows that the S parameters of Br-doped samples are lower than that of $FAPbI_3$. This indicates the vacancy densities including cation and anion vacancies of Br-doped samples are lower than that of $FAPbI_3$. The incorporation of small halogen anions leads to the lattice strain relaxation that will prevent the formation of defects [60]. This is caused by the ionic size mismatch between the A cation and the lead halide. From figures 6(a) and (b), we can see the S parameters of the $FAPb(I_{1-x}Br_x)_3$ samples with $x = 0.05$, 0.15, and 0.2 are close to each other. This suggests that the defect densities of these three samples are almost the same. This is reasonable considering that the effect of lattice strain relaxation is not obvious when Br contents are low. When Br content is in the range of 0.3–0.4, about one-third of iodine is replaced by Br. The lattice strain relaxation is hence significant and the defect densities decreased dramatically. This is indicated by the relative S parameter evolution in figure 6(b). The lattice strain can also change the PbX_6 connection from corner-sharing to edge-sharing which yields a lower α/δ phase content ratio when Br content is high. The change of phase composition may influence the defect densities of $FAPb(I_{1-x}Br_x)_3$ samples.

3.5. Influence of Br on photovoltaic performance

The photovoltaic performance of perovskite films with different Br content was checked by current density–voltage (J–V) characteristics. A mesoscopic structure was used as illustrated in figure 7(a). To check the influence of Br-doping on the film thicknesses of perovskite layers, the cross-section morphology of incomplete devices without spiro-OMeTAD and Ag back contact was checked (figure S5). As a result, a perovskite layer thickness of 500–600 nm was observed in all devices with negligible difference. The influence of active layer difference could hence be excluded in discussing the photovoltaic performance. The thicknesses of c-TiO_2 and m-TiO_2 in this work were about 60 and 150 nm, respectively. The J–V curves of PSCs with different perovskite films are shown in figure 7(b). The corresponding photovoltaic parameters are listed in table S1. With the increase of Br content, higher open circuit voltage (V_{OC}) was observed. For short circuit current density (J_{SC}), a maximum value was obtained with $x = 0.05$ in perovskite film. The change of V_{OC} is a result of bandgap and defect density differences. With wider bandgap and lower recombination caused by trap-assisted non-radiative recombination [61], PSCs based on high Br content achieved larger V_{OC} values. The J_{SC} of these devices depends on the absorption range of the solar spectrum (bandgap of perovskite films) and the perovskite phase content. The available light range decreases with the increase of Br content and the perovskite phase content is determined by

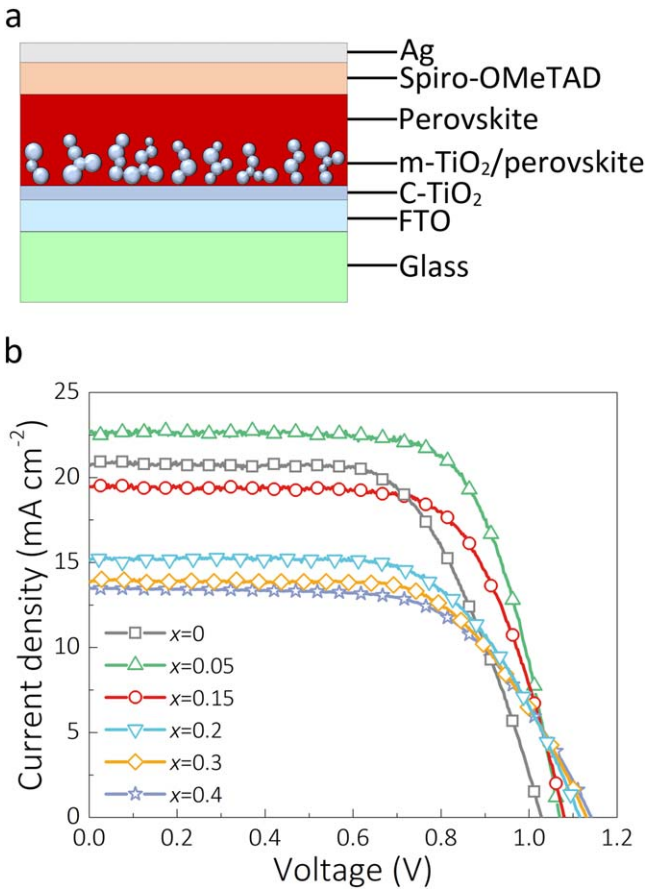

Figure 7. *J–V* characteristics of PSCs based on $FAPb(I_{1-x}Br_x)_3$ films.

the stability. The best photovoltaic performance was achieved with a Br content of 0.05. Compared to pristine $FAPbI_3$, the PCE of PSC based on $FAPb(I_{0.95}Br_{0.05})_3$ increased by 25.7%.

4. Conclusions

The effect of Br-doping on phase stability and performance of $FAPb(I_{1-x}Br_x)_3$ films was studied in this paper. The phase stability is closely correlated to Br content. Incorporating a low content of Br can stabilize the perovskite phase. However, the stability of α phase notably decreases with high Br content. The origin of low phase stability is attributed to the serious tilt and distortion of the PbI_6 octahedral framework and the shrinkage of the interstitial sites. According to SEM measurements, pristine $FAPbI_3$ film has a rough surface with a small average grain size, while each Br-doped sample has a flat surface with a larger average grain size. This indicates that the introduction of Br enhances the morphology of the films. The maximum size of surface grains of 287.3 nm was obtained with a Br content of 0.15. Both the element mapping and perovskite phase lattice parameter indicate the homogeneous distribution of Br in α and δ phases. The bandgaps and energy level position trends of $FAPb(I_{1-x}Br_x)_3$ were clarified. The Fermi level and VB maximum downshift with the increase of Br content. They are probably attributed to the decrease of halide vacancy densities and the increase of Br 4*p* orbital content in VB. The defect information in the films is analyzed by positron annihilation measurements. Lower defect densities are observed in higher Br content samples. The photovoltaic performance of $FAPb(I_{1-x}Br_x)_3$ films were clarified. Owing to the high phase stability, enhanced morphology and low defect density, $FAPb(I_{0.95}Br_{0.05})_3$ film achieved the best photoelectric conversion efficiency of 17.12%.

Acknowledgments

This work was financially supported by the National Natural Science Foundation of China (Grant No. 11475165, 11775215, 11875248), the National High Technology Research and Development Program of China (Grant No. 2014AA052002), Science and Technology Service Network Initiative of the Chinese Academy of Sciences (KFJ-SW-STS-152), Shanghai Municipal Natural Science Foundation (Grant No. 16ZR1441000), Shanghai Municipal Sciences and Technology Commission (Grant No. 12DZ1203900) and the Shanghai High & New Technology's Industrialization Major Program (Grant No. 2013-2).

Conflict of interest

The authors declare no conflict of interest.

ORCID iDs

Xiaojie Ni https://orcid.org/0000-0002-8903-4834
Lei Lei https://orcid.org/0000-0002-0068-310X
Songwang Yang https://orcid.org/0000-0001-6304-5941

References

[1] Chen S, Lei L, Yang S, Liu Y and Wang Z S 2015 Characterization of perovskite obtained from two-step deposition on mesoporous titania *ACS Appl. Mater. Interfaces* **7** 25770–6
[2] Huang A, Lei L, Zhu J, Yu Y, Liu Y, Yang S, Bao S, Cao X and Jin P 2017 Fast fabrication of a stable perovskite solar cell with an ultrathin effective novel inorganic hole transport layer *Langmuir* **33** 3624–34
[3] Wu Y, Yang X, Chen W, Yue Y, Cai M, Xie F, Bi E, Islam A and Han L 2016 Perovskite solar cells with 18.21% efficiency and area over 1 cm^2 fabricated by heterojunction engineering *Nat. Energy* **1** 16148
[4] Yang W S, Noh J H, Jeon N J, Kim Y C, Ryu S, Seo J and Seok S I 2015 High-performance photovoltaic perovskite layers fabricated through intramolecular exchange *Science* **348** 1234–7
[5] Li X, Bi D, Yi C, Décoppet J-D, Luo J, Zakeeruddin S M, Hagfeldt A and Grätzel M 2016 A vacuum flash–assisted solution process for high-efficiency large-area perovskite solar cells *Science* **353** 58–62
[6] Bi D *et al* 2016 Efficient luminescent solar cells based on tailored mixed-cation perovskites *Sci. Adv.* **2** e1501170

[7] Yu S, Yan Y, Chen Y, Chábera P, Zheng K and Liang Z 2019 nabling room-temperature processed highly efficient and stable 2D Ruddlesden–Popper perovskite solar cells with eliminated hysteresis by synergistic exploitation of additives and solvents *J. Mater. Chem.* A **7** 2015–21

[8] Kim H S *et al* 2012 Lead iodide perovskite sensitized all-solid-state submicron thin film mesoscopic solar cell with efficiency exceeding 9% *Sci. Rep.* **2** 591

[9] Baikie T, Fang Y, Kadro J M, Schreyer M, Wei F, Mhaisalkar S G, Graetzel M and White T J 2013 Synthesis and crystal chemistry of the hybrid perovskite $(CH_3NH_3)PbI_3$ for solid-state sensitised solar cell applications *J. Mater. Chem.* A **1** 5628–41

[10] Burschka J, Pellet N, Moon S J, Humphry-Baker R, Gao P, Nazeeruddin M K and Grätzel M 2013 Sequential deposition as a route to high-performance perovskite-sensitized solar cells *Nature* **499** 316–9

[11] Chen Q, Zhou H, Hong Z, Luo S, Duan H S, Wang H H, Liu Y, Li G and Yang Y 2014 Planar heterojunction perovskite solar cells via vapor-assisted solution process *J. Am. Chem. Soc.* **136** 622–5

[12] Choi J J, Yang X, Norman Z M, Billinge S J and Owen J S 2014 Structure of methylammonium lead iodide within mesoporous titanium dioxide: active material in high-performance perovskite solar cells *Nano Lett.* **14** 127–33

[13] Docampo P, Ball J M, Darwich M, Eperon G E and Snaith H J 2013 Efficient organometal trihalide perovskite planar-heterojunction solar cells on flexible polymer substrates *Nat. Commun.* **4** 2761

[14] Heo J H *et al* 2013 Efficient inorganic–organic hybrid heterojunction solar cells containing perovskite compound and polymeric hole conductors *Nat. Photon.* **7** 486–91

[15] Jeng J Y, Chiang Y F, Lee M H, Peng S R, Guo T F, Chen P and Wen T C 2013 $CH_3NH_3PbI_3$ perovskite/fullerene planar-heterojunction hybrid solar cells *Adv. Mater.* **25** 3727–32

[16] Ku Z, Rong Y, Xu M, Liu T and Han H 2013 Full printable processed mesoscopic $CH_3NH_3PbI_3/TiO_2$ heterojunction solar cells with carbon counter electrode *Sci. Rep.* **3** 3132

[17] Kumar M H, Yantara N, Dharani S, Graetzel M, Mhaisalkar S, Boix P P and Mathews N 2013 Flexible, low-temperature, solution processed ZnO-based perovskite solid state solar cells *Chem. Commun.* **49** 11089–91

[18] Im J H, Jang I H, Pellet N, Grätzel M and Park N G 2014 Growth of $CH_3NH_3PbI_3$ cuboids with controlled size for high-efficiency perovskite solar cells *Nat. Nanotechnol.* **9** 927–32

[19] Heo J H, Han H J, Kim D, Ahn T K and Im S H 2015 Hysteresis-less inverted $CH_3NH_3PbI_3$ planar perovskite hybrid solar cells with 18.1% power conversion efficiency *Energy Environ. Sci.* **8** 1602–8

[20] Yu Y, Yang S, Lei L and Liu Y 2017 Nucleation mediated interfacial precipitation for architectural perovskite films with enhanced photovoltaic performance *Nanoscale* **9** 2569–78

[21] Yu Y, Yang S, Lei L, Cao Q, Shao J, Zhang S and Liu Y 2017 Ultrasmooth perovskite film via mixed anti-solvent strategy with improved efficiency *ACS Appl. Mater. Interfaces* **9** 3667–76

[22] Si H, Liao Q, Zhang Z, Li Y, Yang X, Zhang G, Kang Z and Zhang Y 2016 An innovative design of perovskite solar cells with Al_2O_3 inserting at ZnO/perovskite interface for improving the performance and stability *Nano Energy* **22** 223–31

[23] Si H, Liao Q, Kang Z, Ou Y, Meng J, Liu Y, Zhang Z and Zhang Y 2017 Deciphering the NH_4PbI_3 intermediate phase for simultaneous improvement on nucleation and crystal growth of perovskite *Adv. Funct. Mater.* **27** 1701804

[24] Koh T M, Fu K, Fang Y, Chen S, Sum T C, Mathews N, Mhaisalkar S G, Boix P P and Baikie T 2013 Formamidinium-containing metal-halide: an alternative material for Near-IR absorption perovskite solar cells *J. Phy. Chem.* C **118** 16458–62

[25] Lee J-W, Kim D-H, Kim H-S, Seo S-W, Cho S M and Park N-G 2015 Formamidinium and cesium hybridization for photo- and moisture-stable perovskite solar cell *Adv. Energy Mater.* **5** 1501310

[26] Saliba M *et al* 2016 Incorporation of rubidium cations into perovskite solar cells improves photovoltaic performance *Science* **354** 206–9

[27] Lee J W, Seol D J, Cho A N and Park N G 2014 High-efficiency perovskite solar cells based on the black polymorph of $HC(NH_2)_2PbI_3$ *Adv. Mater.* **26** 4991–8

[28] Bella F, Griffini G, Correa-Baena J-P, Saracco G, Grätzel M, Hagfeldt A, Turri S and Gerbaldi C 2016 Improving efficiency and stability of perovskite solar cells with photocurable fluoropolymers *Science* **354** 203–6

[29] Bi D, Yi C, Luo J, Décoppet J-D, Zhang F, Zakeeruddin Shaik M, Li X, Hagfeldt A and Grätzel M 2016 Polymer-templated nucleation and crystal growth of perovskite films for solar cells with efficiency greater than 21% *Nat. Energy* **1** 16142

[30] Hu M, Liu L, Mei A, Yang Y, Liu T and Han H 2014 Efficient hole-conductor-free, fully printable mesoscopic perovskite solar cells with a broad light harvester $NH_2CH{=}NH_2PbI_3$ *J. Mater. Chem.* A **2** 17115–21

[31] Yang W S *et al* 2017 Iodide management in formamidinium-lead-halide–based perovskite layers for efficient solar cells *Science* **356** 1376–9

[32] Jiang Q, Zhang L, Wang H, Yang X, Meng J, Liu H, Yin Z, Wu J, Zhang X and You J 2016 Enhanced electron extraction using SnO_2 for high-efficiency planar-structure $HC(NH_2)_2PbI_3$-based perovskite solar cells *Nat. Energy* **2** 16117

[33] Kim J, Yun J S, Wen X, Soufiani A M, Lau C F J, Wilkinson B, Seidel J, Green M A, Huang S and Ho-Baillie A W Y 2016 Nucleation and growth control of $HC(NH_2)_2PbI_3$ for planar Perovskite solar cell *J. Phys. Chem.* C **120** 11262–7

[34] Long M *et al* 2017 Large-grain formamidinium $PbI_{3-x}Br_x$ for high-performance perovskite solar cells via intermediate halide exchange *Adv. Energy Mater.* **7** 1601882

[35] Xie J, Liu Y, Liu J, Lei L, Gao Q, Li J and Yang S 2015 Study on the correlations between the structure and photoelectric properties of $CH_3NH_3PbI_3$ perovskite light-harvesting material *J. Power Sources* **285** 349–53

[36] Jesper Jacobsson T, Correa-Baena J-P, Pazoki M, Saliba M, Schenk K, Grätzel M and Hagfeldt A 2016 Exploration of the compositional space for mixed lead halogen perovskites for high efficiency solar cells *Energy Environ. Sci.* **9** 1706–24

[37] Shockley W and Queisser H J 1961 Detailed balance limit of efficiency of p–n junction solar cells *J. Appl. Phys.* **32** 510–9

[38] Pang S, Hu H, Zhang J, Lv S, Yu Y, Wei F, Qin T, Xu H, Liu Z and Cui G 2014 $NH_2CH{=}NH_2PbI_3$: an alternative organolead iodide perovskite sensitizer for mesoscopic solar cells *Chem. Mater.* **26** 1485–91

[39] Smecca E, Numata Y, Deretzis I, Pellegrino G, Boninelli S, Miyasaka T, La Magna A and Alberti A 2016 Stability of solution-processed $MAPbI_3$ and $FAPbI_3$ layers *Phys. Chem. Chem. Phys.* **18** 13413–22

[40] Yao D, Zhang C, Pham N D, Zhang Y, Tiong V T, Du A, Shen Q, Wilson G J and Wang H 2018 Hindered formation of photoinactive delta-$FAPbI_3$ phase and hysteresis-free mixed-cation planar heterojunction perovskite solar cells with enhanced efficiency via potassium incorporation *J. Phys. Chem. Lett.* **9** 2113–20

[41] Chen T, Foley B J, Park C, Brown C M, Harriger L W, Lee J, Ruff J, Yoon M, Choi J J and Lee S-H 2016 Entropy-driven structural transition and kinetic trapping in formamidinium lead iodide perovskite *Sci. Adv.* **2** e1601650
[42] Binek A, Hanusch F C, Docampo P and Bein T 2015 Stabilization of the trigonal high-temperature phase of formamidinium lead iodide *J. Phys. Chem. Lett.* **6** 1249–53
[43] Aguiar J A, Wozny S, Holesinger T G, Aoki T, Patel M K, Yang M, Berry J J, Al-Jassim M, Zhou W and Zhu K 2016 *In situ* investigation of the formation and metastability of formamidinium lead tri-iodide perovskite solar cells *Energy Environ. Sci.* **9** 2372–82
[44] Yun J S, Kim J, Young T, Patterson R J, Kim D, Seidel J, Lim S, Green M A, Huang S and Ho-Baillie A 2018 Humidity-Induced degradation via grain boundaries of $HC(NH_2)_2PbI_3$ planar perovskite solar cells *Adv. Funct. Mater.* **28** 1705363
[45] Weller M T, Weber O J, Frost J M and Walsh A 2015 Cubic perovskite structure of black formamidinium lead iodide, α-$[HC(NH_2)_2]PbI_3$, at 298 K *J. Phys. Chem. Lett.* **6** 3209–12
[46] Jeon N J, Noh J H, Yang W S, Kim Y C, Ryu S, Seo J and Seok S I 2015 Compositional engineering of perovskite materials for high-performance solar cells *Nature* **517** 476–80
[47] Yi C, Luo J, Meloni S, Boziki A, Ashari-Astani N, Grätzel C, Zakeeruddin S M, Röthlisberger U and Grätzel M 2016 Entropic stabilization of mixed A-cation ABX_3 metal halide perovskites for high performance perovskite solar cells *Energy Environ. Sci.* **9** 656–62
[48] Veen A V, Schut H, Vries J d, Hakvoort R A and Ijpma M R 1991 Analysis of positron profiling data by means of 'VEPFIT' *AIP Conf. Proc.* **218** 171–98
[49] Veen A V, Schut H, Clement M, De N J, Kruseman A and Ijp-ma M 1995 Vepfit applied to depth profiling problems *Appl. Surf. Sci.* **85** 216–24
[50] Zhumekenov A A *et al* 2016 Formamidinium lead halide perovskite crystals with unprecedented long carrier dynamics and diffusion length *ACS Energy Lett.* **1** 32–7
[51] Proffit D L, Jang H W, Lee S, Nelson C T, Pan X Q, Rzchowski M S and Eom C B 2008 Influence of symmetry mismatch on heteroepitaxial growth of perovskite thin films *Appl. Phys. Lett.* **93** 111912
[52] Noh J H, Im S H, Heo J H, Mandal T N and Seok S I 2013 Chemical management for colorful, efficient, and stable inorganic–organic hybrid nanostructured solar cells *Nano Lett.* **13** 1764–9
[53] Eperon G E, Stranks S D, Menelaou C, Johnston M B, Herz L M and Snaith H J 2014 Formamidinium lead trihalide: a broadly tunable perovskite for efficient planar heterojunction solar cells *Energy Environ. Sci.* **7** 982–8
[54] Goldschmidt V M 1926 Die Gesetze der Krystallochemie *Naturwissenschaften* **14** 477–85
[55] Endres J *et al* 2016 Valence and conduction band densities of states of metal halide perovskites: a combined experimental-theoretical study *J. Phys. Chem. Lett.* **7** 2722–9
[56] Dryzek J, Dryzek E, Börner F and Krause-Rehberg R 2001 Subsurface zones created under lubrication conditions studied by positron annihilation *Tribol. Lett.* **11** 29–36
[57] Yu Y, Lei L, Yang S, Xie J, Shao J, Cao Q, Zhang S, Ni X, Ye B and Liu Y 2017 Novel perovskite solar cell architecture featuring efficient light capture and ultrafast carrier extraction *ACS Appl. Mater. Interfaces* **9** 23624–34
[58] Stoumpos C.C., Malliakas C D and Kanatzidis M G 2013 Semiconducting tin and lead iodide perovskites with organic cations: phase transitions, high mobilities, and near-infrared photoluminescent properties *Inorg. Chem.* **52** 9019–38
[59] Jin S, Zhang P, Lu E, Guo L, Wang B and Cao X 2016 Correlation between Cu precipitates and irradiation defects in Fe–Cu model alloys investigated by positron annihilation spectroscopy *Acta Mater.* **103** 658–64
[60] Saidaminov M I *et al* 2018 Suppression of atomic vacancies via incorporation of isovalent small ions to increase the stability of halide perovskite solar cells in ambient air *Nat. Energy* **3** 648–54
[61] Wetzelaer G, Scheepers M, Sempere A, Momblona C and Ávila H B J 2015 Trap-assisted non-radiative recombination in organic–inorganic perovskite solar cells *Adv. Mater.* **27** 1837–41